

# Self-dual compactons in the gauged restricted baby Skyrme model with magnetic impurity

N. H. Gonzalez-Gutierrez <sup>\*</sup>, Rodolfo Casana <sup>†</sup> and André C. Santos <sup>‡</sup>

*Departamento de Física, Universidade Federal do Maranhão, 65080-805, São Luís, Maranhão, Brazil.*

We investigate the existence of compact self-dual solitons in the restricted gauged baby Skyrme model in the presence of a magnetic impurity. The consistent implementation of the Bogomol'nyi-Prasad-Sommerfield (BPS) formalism depends on the relative size between the compacton and the impurity. To address this, we analyze the following scenarios: in the first, the impurity is entirely inside the compacton, and in the second, the impurity fully encircles the compacton. In both cases, the approach has enabled us to set the self-dual potential, achieve the Bogomol'ny bound for the energy, and establish the self-dual or BPS equations whose solutions saturate such a bound. We next focused on obtaining radially symmetric compactons, where for such an aim, we chose two types of functions to solve the BPS system: the first defining a step-type impurity and the second a Gaussian impurity. After solving the BPS system numerically, we depicted the resulting field profiles and highlighted the effects induced on the compacton's size, field profiles, magnetic field, and magnetic flux.

## I. INTRODUCTION

Effective field theories play a crucial role in contemporary physics, especially when they offer insights into specific system properties that remain challenging to extract starting from the corresponding high-energy model. One of the most fundamental still unsolved issues in modern theoretical physics is searching for an effective low-energy model derived entirely from Quantum Chromodynamics (QCD). In this context, the (1+3)-dimensional Skyrme model [1] emerges as a promissory effective theory for describing such a regimen [2–16]. This nonlinear model identifies the baryons as collective excitations (i.e., topological solitons called Skyrmions) of the fundamental QCD fields. However, one of the main problems of the Skyrme model is providing binding energies that are one order of magnitude larger than the respective experimental nuclear data [16].

In the face of such a problem, searching for a model embodying a Bogomol'nyi-Prasad-Sommerfield (BPS) structure [17, 18] is a possible starting point for circumventing this problem. Such a class of theories possesses an energy lower-bound (the Bogomol'ny bound) of topological character and stable solitons (solutions of the so-called BPS equations) that saturate such a bound. Since the masses of atomic nuclei are nearly linear on the baryon charge, investigating (near)BPS Skyrmions becomes a convenient approach because the Bogomol'ny bound depends linearly on the topological (baryon) charge, resulting in null classical binding energies. Moreover, adding to the Lagrangian density quantum corrections and small contributions of additional terms, we can achieve realistic small values for nuclear binding energies [19–23].

On the other hand, understanding the (1 + 2)-dimensional version of the Skyrme model, known as the baby Skyrme model [24–28], has led to remarkable advances in comprehending other effective models related to the Skyrme one. The baby Skyrme model describes stable solitons but does not possess a BPS structure. Nevertheless, lacking the sigma model term, the dubbed restricted baby Skyrme model [29] does admit BPS configurations [30–32]. Subsequently, Ref. [33] have initiated the looking for BPS versions of the gauged restricted baby Skyrme model, whose attained solutions carry magnetic flux only, as do those found in Refs. [34, 35]. Similarly, Refs. [36, 37] have performed the search for BPS solitons in the gauged restricted baby Skyrme model immersed in a magnetic medium. Moreover, recent studies have proven that BPS Skyrmions can also carry magnetic flux and electric charge [38–40]. In the same way, Refs. [41–44] have investigated aspects related to supersymmetry and the BPS states, whereas Refs. [45, 46] have analyzed the presence of BPS Skyrmions in gravitational theories.

Recently, the study of topological structures in the presence of impurities has been gaining increasing attention. Including an impurity (a non-dynamical background field) in a physical system is equivalent to embedding the field theory describing it within a nontrivial medium. The impurities may arise or emerge inside a physical system from local inhomogeneities or global dependencies on external parameters. Consequently, physical environments such as condensed matter [47], Bose-Einstein condensates [48, 49], inclusive in neutron stars [50, 51] have been explored to study impurity's effects on topological states. In the framework of self-dual systems, a BPS model coupled to an impurity may, in general, lose its BPS structure completely, i.e., the solitons solutions do not saturate the correspondent BPS bound. However, in Refs. [52–54], the authors have shown that it is possible to construct an impurity model preserving half of the BPS property, resulting in so-called half-BPS solutions, such as revealed by the supersymmetric exten-

<sup>\*</sup> [neyver.hgg@discente.ufma.br](mailto:neyver.hgg@discente.ufma.br); [neyver.hgg@gmail.com](mailto:neyver.hgg@gmail.com)

<sup>†</sup> [rodolfo.casana@ufma.br](mailto:rodolfo.casana@ufma.br); [rodolfo.casana@gmail.com](mailto:rodolfo.casana@gmail.com)

<sup>‡</sup> [andre.cs@discente.ufma.br](mailto:andre.cs@discente.ufma.br); [andre.cavs@hotmail.com](mailto:andre.cavs@hotmail.com)

sions of impurity models defined in (1+1)- and (1+2)-dimensions [55]. Moreover, in the literature, there are well-established studies of BPS systems emerging from gauge field theories enlarged by impurities. For example, in the Maxwell-Higgs scenario [56], Chern-Simons-Higgs model [57], in gauged CP(2) case [58], the interaction between a moving Maxwell-Higgs vortex and a static magnetic impurity [59]. Thus, a natural question in the present context is whether the gauged BPS baby Skyrme model exhibits a self-dual structure in the presence of a magnetic impurity.

The present manuscript aims to implement a BPS formalism allowing us to engender compact solitons starting from the gauged restricted baby Skyrme model coupled to a magnetic impurity. For this purpose, we have organized our results as follows: In Sec. II, we introduce the gauged baby Skyrme model in the presence of a magnetic impurity. Sec. III is devoted to implementing the BPS formalism for the model by regarding the following situations: we first consider that the impurity is located totally inside the compacton (internal impurity case), and in the second scenario, one regards that the compacton is contained entirely inside the impurity (extended impurity case). This way, we successfully achieve the energy lower bound (the Bogomol'ny bound) and the corresponding self-dual or BPS equations whose solutions saturate this bound. Besides, one presents the ansatz for attaining radially symmetric solitons. In Sec. IV, we define the form of the superpotential capable of generating compactons in the presence of a magnetic impurity. Next, we explore the effects of two impurities: the first one involves a step-type function, and the second case incorporates a Gaussian function. Finally, we highlight our results and provide our perspectives in Sec. V.

## II. THE MODEL

We introduce our effective model, which describes the restricted gauge Skyrme model [33] in the presence of a magnetic source term, by taking the Lagrangian

$$L = E_0 \int d^2\mathbf{x} \mathcal{L}, \quad (1)$$

with  $E_0$  defining the energy scale (which we set  $E_0 = 1$  in the remainder of the manuscript), and the Lagrangian density given by

$$\mathcal{L} = -\frac{1}{4g^2} F_{\mu\nu}^2 - \frac{\lambda^2}{4} (D_\mu \vec{\phi} \times D_\nu \vec{\phi})^2 + \Delta B - U(\phi_n, \Delta). \quad (2)$$

The coupling between the gauge field and the Skyrme field is given through the covariant derivative

$$D_\mu \vec{\phi} = \partial_\mu \vec{\phi} + A_\mu (\hat{n} \times \vec{\phi}), \quad (3)$$

being  $\vec{\phi}$  the Skyrme field, which is a three-component vector of scalar fields  $\vec{\phi} = (\phi_1, \phi_2, \phi_3)$  obeying  $\vec{\phi} \cdot \vec{\phi} = 1$ ,

and hence describing the unit sphere  $\mathbb{S}^2$ . The unitary vector  $\hat{n}$  gives a preferential direction in the internal space  $\mathbb{S}^2$ .

The first term in Eq. (2) is the Maxwell term, with  $F_{\mu\nu} = \partial_\mu A_\nu - \partial_\nu A_\mu$ , being  $A_\mu$  the Abelian gauge field and  $g$  the electromagnetic coupling constant. The second contribution is the Skyrme term, where  $\lambda$  is the corresponding coupling constant. In third term, we have the so-called magnetic impurity  $\Delta = \Delta(x)$ , which couples linearly to the magnetic field  $B = F_{12}$ . Lastly, the function  $U(\phi_n, \Delta)$  stands for a potential that also is a function of the magnetic impurity, where  $\phi_n \equiv \hat{n} \cdot \vec{\phi}$ . Moreover, both coupling constants are assumed non-negative, being  $g$  and  $\lambda$  with mass dimension 1 and  $-1$  respectively; the gauge field has mass dimension 1, and the Skyrme field is dimensionless.

The Euler-Lagrange equations obtained from Eq. (2) are

$$\partial_\nu F^{\nu\mu} - g^2 (\delta_2^\mu \partial_1 - \delta_1^\mu \partial_2) \Delta = g^2 j^\mu, \quad (4)$$

$$D_\mu \vec{J}^\mu + \frac{\partial V}{\partial \phi_n} (\hat{n} \times \vec{\phi}) = 0, \quad (5)$$

where  $j^\mu = \hat{n} \cdot \vec{J}^\mu$  is the conserved current density, with  $\vec{J}^\mu$  given by

$$\vec{J}^\mu = \lambda^2 [\vec{\phi} \cdot (D^\mu \vec{\phi} \times D^\rho \vec{\phi})] D_\rho \vec{\phi}. \quad (6)$$

In this study, we focus on time-independent solutions and hence, from (4), we obtain the respective Gauss's law

$$\partial_i (\partial_i A_0) = g^2 \lambda^2 A_0 (\hat{n} \cdot \partial_i \vec{\phi})^2. \quad (7)$$

Here, we observe that Gauss's law is identically satisfied by the gauge condition  $A_0 = 0$ , meaning that the resulting configurations carry only magnetic flux. Furthermore, also from Eq. (4), we can obtain Ampère's law

$$\partial_i (B - g^2 \Delta) + g^2 \lambda^2 (\hat{n} \cdot \partial_i \vec{\phi}) Q = 0, \quad (8)$$

where already we have considered  $A_0 = 0$ . The magnetic field is  $B = F_{12} = \epsilon_{ij} \partial_i A_j$  and the quantity  $Q$  defined as

$$Q = \vec{\phi} \cdot (D_1 \vec{\phi} \times D_2 \vec{\phi}) = q + \epsilon_{ij} A_i (\hat{n} \cdot \partial_j \vec{\phi}), \quad (9)$$

being

$$q = \frac{1}{2} \epsilon_{ij} \vec{\phi} \cdot (\partial_i \vec{\phi} \times \partial_j \vec{\phi}), \quad (10)$$

a quantity related to the topological charge or topological degree (or winding number) of the Skyrme field, which is given

$$\text{deg}[\vec{\phi}] = -\frac{1}{4\pi} \int q d^2\mathbf{x} = N \in \mathbb{Z} \setminus \{0\}. \quad (11)$$

Moreover, the stationary version of the Eq. (5) of the Skyrme field becomes

$$\lambda^2 \epsilon_{ij} D_i (Q D_j \vec{\phi}) + \frac{\partial V}{\partial \phi_n} (\hat{n} \times \vec{\phi}) = 0. \quad (12)$$

The following section is devoted to implementing the BPS formalism to investigate the conditions under which the model (2) engenders self-dual compact configurations. The formalism allows us to determine the self-dual potential, the Bogomol'ny bound for the total energy, and the self-dual equations whose solutions saturate such a bound.

### III. BPS STRUCTURE

Let us construct the BPS structure of the gauged baby Skyrme model in the presence of a magnetic impurity to obtain compact Skyrmions. For such a purpose, we consider the stationary energy density of the model (2) that, under the gauge condition  $A_0 = 0$ , reads as

$$\varepsilon = \frac{1}{2g^2} B^2 - \Delta B + \frac{\lambda^2}{2} Q^2 + U(\phi_n, \Delta). \quad (13)$$

Before continuing, we define the type of magnetic impurity by comparing the size of the region it occupies with the area size of the compacton engendered. Thus, in the subsequent subsections, we regard the following situations: in the first one, the impurity is inside totally in the compacton (we name the internal case), and in the second case, the impurity fully contains the compacton (we name the extended case). We will analyze these problems separately.

#### A. BPS compact Skyrmions in the presence of an internal magnetic impurity

We consider the finite region  $\mathcal{R} \subset \mathbb{R}^2$  where the compactons lives, being  $\partial\mathcal{R}$  the boundary of  $\mathcal{R}$  in which the fields attain the vacuum values when  $\mathbf{x} \in \partial\mathcal{R}$ . Thus, we define the internal impurity as being

$$\Delta(\mathbf{x}) = \begin{cases} \Delta^c(\mathbf{x}) & , \quad \mathbf{x} \in \mathcal{R}_0, \\ 0 & , \quad \mathbf{x} \notin \mathcal{R}_0, \end{cases} \quad (14)$$

where  $\Delta^c(\mathbf{x})$  is an integrable function with domain into the region  $\mathcal{R}_0 \subset \mathcal{R}$ . This way, the impurity must satisfy the boundary condition

$$\lim_{\mathbf{x} \rightarrow \partial\mathcal{R}} \Delta(\mathbf{x}) = 0. \quad (15)$$

Now, we establish the boundary conditions to be satisfied in the model in order to ensure the finite-energy and compact configurations. For this, the energy density (13) at the boundary  $\partial\mathcal{R}$  must obey

$$\lim_{\mathbf{x} \rightarrow \partial\mathcal{R}} \varepsilon(\mathbf{x}) = 0, \quad (16)$$

and, this way, the magnetic field, the quantity  $Q$ , and the potential  $U$  must satisfy the following boundary conditions:

$$\lim_{\mathbf{x} \rightarrow \partial\mathcal{R}} Q = 0, \quad (17)$$

$$\lim_{\mathbf{x} \rightarrow \partial\mathcal{R}} B = 0, \quad \lim_{\mathbf{x} \rightarrow \partial\mathcal{R}} U = 0. \quad (18)$$

By taking the integration of the energy density (13), we obtain the system's total energy

$$E = \int_{\mathcal{R}} d^2\mathbf{x} \left[ \frac{1}{2g^2} B^2 - \Delta B + \frac{\lambda^2}{2} Q^2 + U(\phi_n, \Delta) \right], \quad (19)$$

which, after some algebraic manipulations with the aim to implement the BPS formalism, reads

$$E = \int_{\mathcal{R}} d^2\mathbf{x} \left[ \frac{1}{2g^2} (B - g^2 \Delta \pm \lambda^2 g^2 W)^2 + \frac{\lambda^2}{2} (Q \mp W_{\phi_n})^2 \mp \lambda^2 B W \pm \lambda^2 Q W_{\phi_n} + U - \frac{\lambda^2}{2} W_{\phi_n}^2 - \frac{1}{2} g^2 (\lambda^2 W \mp \Delta)^2 \right], \quad (20)$$

where we have introduced the auxiliary function  $W = W(\phi_n)$ , being  $W_{\phi_n} \equiv \partial W / \partial \phi_n$ , to be determine later. Next, by using  $B = \epsilon_{ij} \partial_i A_j$  and the expression (9), we arrive at

$$E = \int_{\mathcal{R}} d^2\mathbf{x} \left[ \frac{1}{2g^2} (B - g^2 \Delta \pm \lambda^2 g^2 W)^2 + \frac{\lambda^2}{2} (Q \mp W_{\phi_n})^2 \pm \lambda^2 q W_{\phi_n} \mp \lambda^2 \epsilon_{ij} \partial_i (W A_j) + U - \frac{\lambda^2}{2} W_{\phi_n}^2 - \frac{1}{2} g^2 (\lambda^2 W \mp \Delta)^2 \right]. \quad (21)$$

Furthermore, by setting the function  $U(\phi_n, \Delta)$  to be

$$U(\phi_n, \Delta) = \frac{\lambda^2}{2} W_{\phi_n}^2 + \frac{1}{2} g^2 (\lambda^2 W \mp \Delta)^2, \quad (22)$$

the last row in (21) vanishes, with Eq. (22) defining the corresponding BPS potential of the model. Consequently, for the function  $W(\phi_n)$ , the vacuum conditions (15) and (18) allow us to establish the boundary conditions

$$\lim_{\mathbf{x} \rightarrow \partial\mathcal{R}} W = 0, \quad \lim_{\mathbf{x} \rightarrow \partial\mathcal{R}} W_{\phi_n} = 0. \quad (23)$$

Henceforth, we shall call  $W(\phi_n)$  of superpotential due to similarities of the relation between potential and superpotential in supersymmetric field theories. In what follows, we observe the contribution of the total derivative  $\epsilon_{ij} \partial_i (W A_j)$  for the energy (21) becomes null due to the boundary condition (23). Therefore, by considering all the previous findings, we express the total energy as

$$E = E_{\text{BPS}} + \bar{E}, \quad (24)$$

where, by using (10), we have defined the Bogomol'ny bound

$$E_{\text{BPS}} = \mp \lambda^2 \int_{\mathcal{R}} d^2 \mathbf{x} W_{\phi_n} \vec{\phi} \cdot (\partial_1 \vec{\phi} \times \partial_2 \vec{\phi}) \geq 0, \quad (25)$$

and  $\bar{E}$  being the integral just of the quadratic terms

$$\bar{E} = \int_{\mathcal{R}} d^2 \mathbf{x} \left[ \frac{1}{2g^2} (B - g^2 \Delta \pm \lambda^2 g^2 W)^2 + \frac{\lambda^2}{2} (Q \mp W_{\phi_n})^2 \right]. \quad (26)$$

Consequently, the total energy (24) satisfies the inequality  $E \geq E_{\text{BPS}}$  and the Bogomol'ny bound will be attained when the fields have configurations such that  $\bar{E} = 0$ , i.e., the bound is saturated when the following set of first-order differential equations obey

$$B = g^2 \Delta \mp \lambda^2 g^2 W, \quad (27)$$

$$Q = \pm W_{\phi_n}, \quad (28)$$

defining the so-called self-dual or BPS equations of the model. Such a set of equations recovers the Euler-Lagrange equations (8) and (12), associated with the Lagrangian density (2) by considering the self-dual potential (22). Furthermore, the solutions of these equations are also classical solutions belonging to an extended supersymmetric model [60, 61] whose bosonic sector would be given by the Lagrangian density (2). Indeed, the gauged restricted baby Skyrme model supports a  $\mathcal{N} = 2$  supersymmetric formulation [62], which is also realizable in the presence of an impurity term [55].

Here, it is essential to point out that if the magnetic impurity does not meet the conditions (14) and (15), then the ones established in (18) for the magnetic field and the potential not be upheld. Such a situation may occur when the impurity extends in space beyond the compact boundary  $\partial\mathcal{R}$ . In this case, it is necessary to define new boundary conditions consistent with the new impurity's configuration. This new circumstance will be discussed to follow.

### B. BPS compact Skyrmions in the presence of an extended magnetic impurity

To study the effects of a magnetic impurity occupying a region  $\mathcal{R}_0 \subseteq \mathbb{R}^2$  that is larger or equal than the one  $\mathcal{R}$  covered by compacton ( $\mathcal{R}$ ), we here consider an impurity function  $\Delta(\mathbf{x})$  obeying the condition

$$\left| \int_{\mathcal{R}_0} \Delta(\mathbf{x}) d^2 \mathbf{x} \right| < \infty, \quad (29)$$

such that  $\mathcal{R} \subseteq \mathcal{R}_0$ .

Now let us establish the boundary conditions to be satisfied by the fields in the presence of the impurity defined

by Eq. (29) to guarantee that the energy density (13) be null at compacton's boundary  $\partial\mathcal{R}$  such as required by the equation (16). Firstly, the boundary condition for the quantity  $Q$  remains being

$$\lim_{\mathbf{x} \rightarrow \partial\mathcal{R}} Q = 0, \quad (30)$$

while the magnetic field and the potential satisfy, respectively, the nonnull conditions

$$\lim_{\mathbf{x} \rightarrow \partial\mathcal{R}} B = g^2 \lim_{\mathbf{x} \rightarrow \partial\mathcal{R}} \Delta, \quad \lim_{\mathbf{x} \rightarrow \partial\mathcal{R}} U = \frac{g^2}{2} \lim_{\mathbf{x} \rightarrow \partial\mathcal{R}} \Delta^2, \quad (31)$$

where the potential at the frontier has to attain its absolute minimum. Thus, these new boundary conditions guarantee that energy density is null when  $x \in \partial\mathcal{R}$ .

Once we have fixed the new boundary conditions, the implementation of the BPS formalism will run similarly to the one developed previously. In this way, the boundary conditions (23) established for the superpotential remain the same. Accordingly, the equations describing the BPS configurations hold their mathematical form, i.e., the BPS potential (22), BPS total energy (25) and the BPS equations (27)-(28) do not change their functional or algebraic structure.

### C. Magnetic flux

An important study is to analyze the effects of the impurity on the magnetic flux. For that, we must measure such an effects in a way that enables us to compare it to flux obtained in the absence of the impurity. With this aim, we begin defining an effective magnetic field from the BPS equation (27) as being

$$B_{\text{eff}} \equiv B - g^2 \Delta = \mp \lambda^2 g^2 W, \quad (32)$$

accounting for the changes in the magnetic flux due to the presence of the impurity. We now define the effective magnetic flux inside the region  $\mathcal{R}$  occupied by the compacton as,

$$\Phi_{\text{eff}} = \int_{\mathcal{R}} B_{\text{eff}} d^2 \mathbf{x} = \Phi_B - \Phi_{\Delta}, \quad (33)$$

where  $\Phi_B$  provides the total magnetic flux,

$$\Phi_B = \int_{\mathcal{R}} B d^2 \mathbf{x}, \quad (34)$$

and the  $\Phi_{\Delta}$  gives the impurity's contribution,

$$\Phi_{\Delta} = g^2 \int_{\mathcal{R}} \Delta d^2 \mathbf{x}. \quad (35)$$

We also can directly compute the effective magnetic flux in the presence of an internal or extended impurity through the integral

$$\Phi_{\text{eff}} = \mp \lambda^2 g^2 \int_{\mathcal{R}} W d^2 \mathbf{x}. \quad (36)$$

It is interesting highlight that the effective magnetic flux (33) is associated with the existence of a magnetization [63]. This correlation exists exactly due to the role played by impurity factor as an external magnetic field, and, this way, the BPS compact Skyrmions described here must have a nonlinear ferromagnetic behavior. In Refs. [63, 64] was performed a detailed study featuring the magnetothermodynamics properties and phase transitions of the BPS-gauged baby Skyrme model under a constant external magnetic field..

#### D. Radially symmetric Skyrmions

Let us now to study the compact Skyrmions possessing a radial symmetry. Thus, the region  $\mathcal{R}$  will be a circle of radius  $R$  defining the compacton's size. Then, without loss generality, we set the unitary vector as  $\hat{n} = (0, 0, 1)$  such that  $\phi_n = \phi_3$ , and we assume the hedgehog ansatz for the Skyrme field

$$\vec{\phi}(r, \theta) = \begin{pmatrix} \sin f(r) \cos N\theta \\ \sin f(r) \sin N\theta \\ \cos f(r) \end{pmatrix}, \quad (37)$$

being  $r$  and  $\theta$  polar coordinates,  $N = \text{deg}[\vec{\phi}]$  the winding number introduced in (11), and  $f(r)$  a regular function satisfying the boundary conditions

$$f(0) = \pi, \quad f(R) = 0. \quad (38)$$

We now redefine the  $\phi_3$  field [33] as

$$\phi_3 = \cos f \equiv 1 - 2h, \quad (39)$$

with the field  $h = h(r)$  obeying

$$h(0) = 1, \quad h(R) = 0. \quad (40)$$

For the gauge field we consider the ansatz

$$A_i(\mathbf{x}) = -\epsilon_{ij} x_j \frac{Na}{r^2}, \quad (41)$$

where  $a = a(r)$  is a well-behaved function that satisfies the boundary conditions

$$a(0) = 0, \quad a(R) = a_R, \quad (42)$$

being  $a_R$  a finite constant.

Taking these considerations, the BPS equations are written as

$$B = \frac{N}{r} \frac{da}{dr} = g^2 \Delta \mp \lambda^2 g^2 W, \quad (43)$$

$$Q = \frac{2N}{r} (1 + a) \frac{dh}{dr} = \mp \frac{1}{2} W_h, \quad (44)$$

where  $W_h = dW/dh$  and with the magnetic impurity being a function depending solely on the radial coordinate,

$\Delta(\mathbf{x}) \equiv \Delta(r)$ . The superpotential  $W(h)$  is a smooth function satisfying the boundary conditions

$$\lim_{r \rightarrow 0} W(h) = W_0, \quad \lim_{r \rightarrow R} W(h) = 0, \quad \lim_{r \rightarrow R} W_h = 0, \quad (45)$$

being  $W_0$  a positive constant.

Further, the corresponding BPS potential (22) results

$$U(h, \Delta) = \frac{\lambda^2}{8} W_h^2 + \frac{1}{2} g^2 (\lambda^2 W \mp \Delta)^2, \quad (46)$$

and the BPS energy density reads

$$\varepsilon_{\text{BPS}} = \frac{\lambda^2}{4} W_h^2 + \lambda^4 g^2 W^2 \mp \lambda^2 g^2 \Delta W. \quad (47)$$

We observe here that the BPS potential and energy density associated with the gauged BPS baby Skyrme model are recovered in the absence of magnetic impurity [33]. Also, we have the Bogomol'ny bound (25) given by

$$E_{\text{BPS}} = \pm 2\pi \lambda^2 N W_0, \quad (48)$$

where the upper (lower) sign corresponds to positive (negative) winding number  $N$  describing the Skyrmions (anti-Skyrmions) configurations.

For the total magnetic flux (34) we get

$$\Phi_B = 2\pi N a_R, \quad (49)$$

where the parameter  $a_R \in \mathbb{R}$  can be computed numerically or, in specific cases, obtained analytically [33]. Further, to conduct a detailed study as an afterthought, it is interesting to seek an expression providing the behavior of the constant  $a_R$ . In this sense, starting from the BPS equations (27) and (28), by using the respective boundary conditions and after some algebraic manipulation, we obtain

$$a_R = -1 + \exp(-g^2 \lambda^2 I_W \mp g^2 I_\Delta), \quad (50)$$

where the parameter  $I_W$  depending on only of the superpotential has been defined as

$$I_W = \int_0^1 \frac{4W}{W_h} dh, \quad (51)$$

whereas  $I_\Delta$  standing for the contribution coming from the magnetic impurity is given by

$$I_\Delta = \int_0^R \frac{4\Delta}{W_h} \left( \frac{dh}{dr} \right) dr. \quad (52)$$

In the following sections, we perform a detailed analysis of the main features presented by the compact BPS Skyrmions, including numerical solutions in which we describe new effects and properties physical. For this, we fix a superpotential capable of engendering compact solutions and select some magnetic impurities.

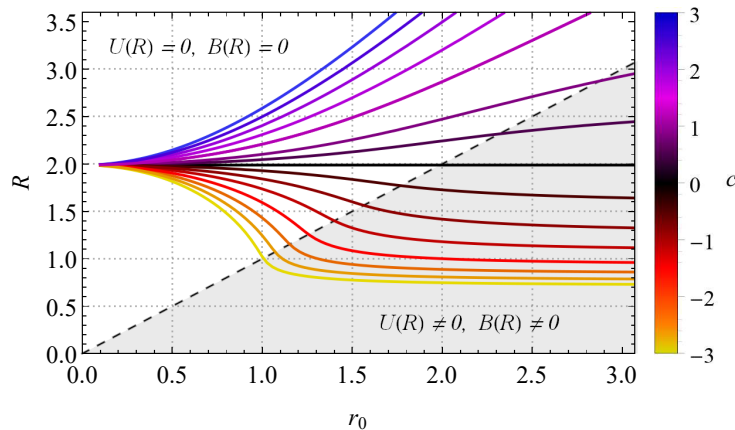


FIG. 1. The compacton's radius  $R$  as a function of the impurity radius  $r_0$  for the impurity function (56) when one fixes  $d = 1.3$  and varies  $c$  values. The dashed line delimits the solutions for the internal impurity (upper region) and extended impurity (lower region). The value  $c = 0$  (black line) stands for BPS compact Skyrmions obtained when the magnetic impurity is absent. We also have fixed the values  $N = 1$ ,  $\lambda = 1$ , and  $g = 1$ .

#### IV. COMPACT SKYRMIONS IN THE PRESENCE OF SOME MAGNETIC IMPURITIES

Once our study is focused only on compact Skyrmions, we consider the following superpotential

$$W(h) = W_0 h^\gamma, \quad 1 < \gamma < 2, \quad (53)$$

where such a constraint to  $\gamma$  values ensure the existence of the compactons. One points out that although we here assume the  $\gamma$  values restricted by Eq. (53), such a superpotential also supports non-compact solitons for  $\gamma \geq 2$ , as reported in the literature.[35, 37, 39, 40].

In what follows, we choose the following superpotential

$$W(h) = \frac{h^{3/2}}{\lambda^2}, \quad (54)$$

which induces a BPS potential (46) that behaves as  $U \sim h$  when  $r \rightarrow R$ , with  $R$  defining the compacton radius. The potential vacuum behavior recalls the so-called ‘‘old baby Skyrme potential’’ that also engenders compact Skyrmions [33, 65].

The BPS bound (48) under the considerations above leads to

$$E_{\text{BPS}} = \pm 2\pi N, \quad (55)$$

being therefore quantized in units of  $2\pi$ . Hereafter, without loss of generality, we will take the upper sign associated with the positive winding number  $N$  describing the Skyrmions configurations.

##### A. Step-type impurity

We follow our analysis by considering the magnetic impurity described by the step-type function

$$\Delta(r) = c \left(1 - \frac{r^2}{r_0^2}\right)^d \theta(r_0 - r), \quad (56)$$

where the parameters  $c \in \mathbb{R}$ ,  $d \geq 0$ , and  $r_0 > 0$  control the magnetic impurity features. The function  $\theta(r_0 - r)$  stands for the step function, with  $r_0$  defining the impurity's radius. The main motivation for choosing the function (56) is the possibility to describe the two impurity scenarios introduced in Sec. III, allowing us to explore the different effects on compact Skyrmions. Thereby, the impurity (56) supports both conditions (14) and (29), i.e.,

- (i) for  $r_0 < R$ , its domain satisfies the condition  $\mathcal{R}_0 \subset \mathcal{R}$  describing a magnetic impurity located totally inside the compact Skyrmion (see Sec. III A); and
- (ii) for  $r_0 > R$ , its domain fulfills  $\mathcal{R} \subset \mathcal{R}_0$  depicting a magnetic impurity whose radius is larger than that of the compacton (see Sec. III B).

Then, by regarding the superpotential (54) and the impurity function (56), the corresponding BPS equations (43) and (44) reads as

$$\frac{N}{r} \frac{da}{dr} + g^2 h^{3/2} - g^2 c \left(1 - \frac{r^2}{r_0^2}\right)^d \theta(r_0 - r) = 0, \quad (57)$$

$$N \frac{(1+a)}{r} \frac{dh}{dr} + \frac{3}{8\lambda^2} h^{1/2} = 0. \quad (58)$$

We present below the behavior of the field profiles near the boundaries, i.e., at  $r = 0$  and  $r = R$ , and the numerical solutions attained by solving the BPS equations (57) and (58), under boundary conditions (40) and (42).

##### 1. The compacton radius

Firstly, one presents how the compacton's radius behaves regarding the impurity parameters. This way, the

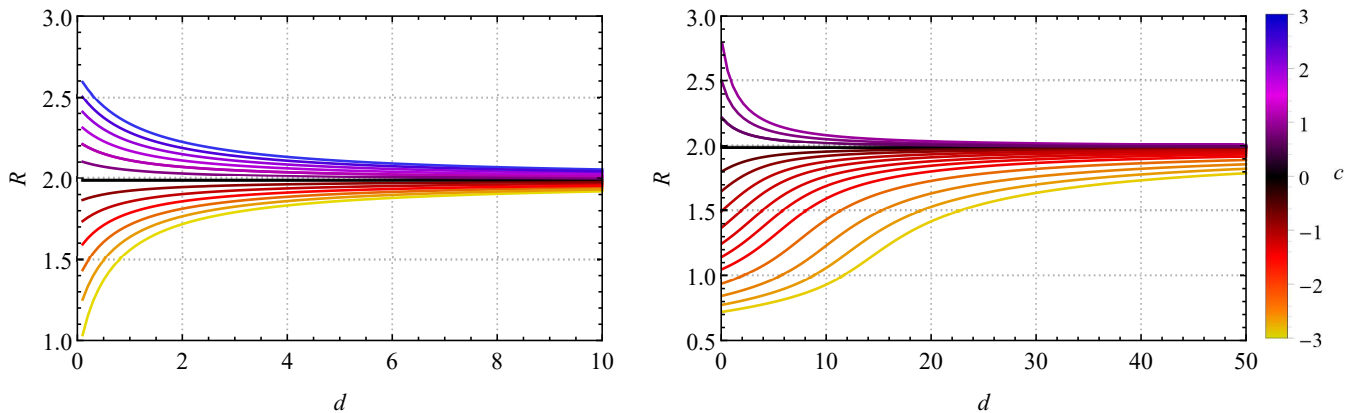


FIG. 2. The compacton's radius  $R$  as a function of the parameter  $d$  with different  $c$  values for the impurity function (56), where we have assumed  $r_0 = 0.7$  (left panel) for internal impurity ( $r_0 < R$ ) and  $r_0 = 2.5$  (right panel) for extended impurity ( $r_0 > R$ ). The value  $c = 0$  (black line) represents the BPS compact Skyrmions without magnetic impurity. We also have fixed the values  $N = 1$ ,  $\lambda = 1$ , and  $g = 1$ .

Fig. 1 depicts the compacton's radius  $R$  vs.  $r_0$ , showing the effects of the impurity (56) on the compacton's size when the impurity radius ( $r_0$ ) varies by considering a fixed value for  $d$  (here = 1.3) and different values  $c$ . Besides, there is highlighted the boundary  $r_0 = R$  (dashed black line) that delimits the regions  $r_0 < R$  and  $r_0 > R$ . The upper region contains the radii of the compact Skyrmions satisfying the boundary conditions (18), and the lower region includes the radii of the ones satisfying the conditions (31). From the figure, we observe that for the case of an internal impurity ( $r_0 < R$ ), there is a minimum value  $c_{\min}$  (here  $\simeq -7.631$ ) such that for  $c > c_{\min}$  the boundary conditions (18) are satisfied. Conversely, for the case of an extended impurity ( $r_0 > R$ ) we have a maximum value  $c_{\max}$  (here  $\simeq 0.316$ ) such that for  $c < c_{\max}$  the boundary conditions (31) are fulfilled. Therefore, the numerical analysis has allowed us to verify that, depending on whether the impurity is internal or extended, not all the  $c$  values are permitted.

Likewise, in Fig. 2, we have presented the compacton's radius  $R$  as a function of the parameter  $d$  by setting  $r_0 = 0.7$  for an internal impurity (left panel) and  $r_0 = 2.5$  for an extended one (right panel). We observe in both cases that, for sufficiently large  $d$  values, the radius of the compact Skyrmion tends to the value attained in the absence of the impurity ( $c = 0$ , black line).

## 2. Compact Skyrmions

Firstly, for the behavior of the Skyrme profile  $h(r)$  near the origin ( $r \rightarrow 0$ ) we get

$$h(r) \approx 1 - \frac{3}{2^4 N \lambda^2} r^2 + \frac{3}{2^6 N^2 \lambda^2} \left[ \frac{3}{2^4 \lambda^2} + g^2(c-1) \right] r^4. \quad (59)$$

Already close to the compacton's border ( $r \rightarrow R$ ), it

behaves as

$$h(r) \approx \mathcal{H}_R \rho^2 - \frac{\mathcal{H}_R}{R} \rho^3, \quad r_0 < R, \quad (60)$$

for the internal impurity, whereas we have for the extended one

$$h(r) \approx \mathcal{H}_R \rho^2 - \frac{\mathcal{H}_R}{R} \left[ 1 - \frac{g^2 R^2 \Delta(R)}{N(1+a_R)} \right] \rho^3, \quad r_0 > R, \quad (61)$$

where  $\rho = R - r \rightarrow 0^+$ , being  $\mathcal{H}_R$  and  $\Delta(R)$  given by

$$\mathcal{H}_R = \frac{9R^2}{2^8 \lambda^4 N^2 (1+a_R)^2}, \quad (62)$$

$$\Delta(R) \equiv \lim_{r \rightarrow R} \Delta(r) = c \left( 1 - \frac{R^2}{r_0^2} \right)^d, \quad (63)$$

respectively.

Then, near the origin, Eq. (59) shows the magnetic impurity has a weak influence on the  $h(r)$  profile, as verified by numerical results shown in the top panels in Fig. 3. In turn, close to the compact's border ( $r = R$ ), the equations (60) and (61), at the  $\rho^3$ -order, illustrate how the Skyrmion's profiles approach to the vacuum value  $h(R) = 0$ . We observe that the internal case has no explicit contribution of the impurity function, as shown by Eq (60), whereas Eq. (61) exhibits the impurity contribution for the extended case. Specifically, in the left panel of Fig. 3, we have considered an internal impurity with radius  $r_0 = 0.7$  and represented the compactons with radius  $R > r_0$ , satisfying the conditions (18), for the  $c > c_{\min}$  allowed values. On the other hand, in the right panel of Fig. 3, we have selected an extended impurity with radius  $r_0 = 2.5$  and shown the compact Skyrmions whose radii satisfy  $R < r_0$  fulfilling the conditions (31), for the  $c < c_{\max}$  allowed values. Furthermore, we again point out that allowed values for the parameter  $c$  depend on the impurity's radius  $r_0$ , which defines whether it is

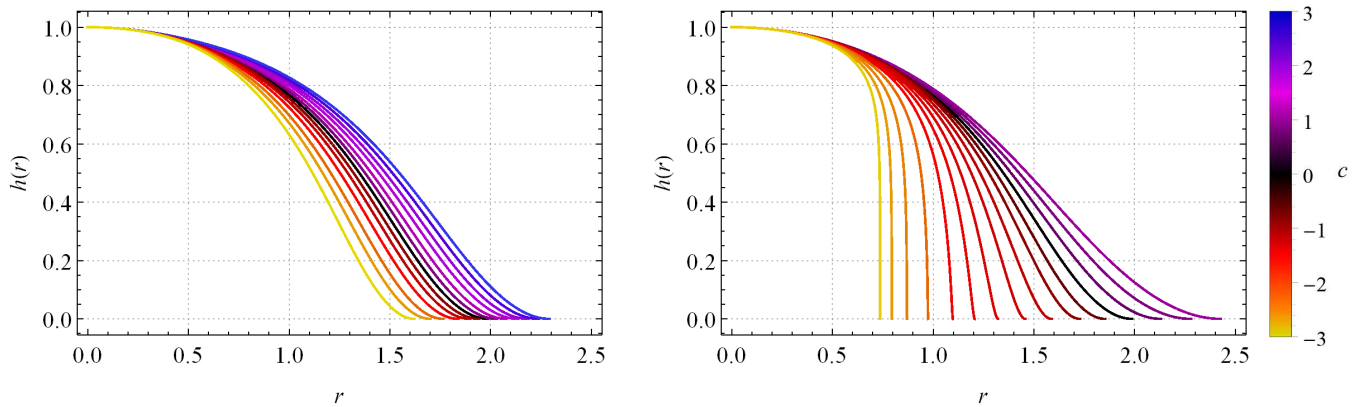


FIG. 3. Skyrmon profiles  $h(r)$  obtained for the impurity function (56). We have considered a fixed  $d = 1.3$  and different values of the parameter  $c$ , with  $r_0 = 0.7$  (left panel) for describing the internal impurity ( $r_0 < R$ ) and  $r_0 = 2.5$  (right panel) for representing the extended impurity ( $r_0 > R$ ). We also have fixed the values  $N = 1$ ,  $\lambda = 1$ , and  $g = 1$ .

internal or extended accordingly established in Sec. III. In addition, the numerical analysis also reveals that the  $c$  parameter controls the size of the compacton, i.e., its radius. The Fig. 1 also shows these features related to the  $c$  parameter.

### 3. Gauge field profiles

For the gauge field, we have the behavior close to the origin given as

$$a(r) \approx \frac{g^2(c-1)}{2N}r^2 + \frac{g^2}{4N} \left( \frac{9}{2^5\lambda^2N} - \frac{cd}{r_0^2} \right) r^4, \quad (64)$$

and near the compacton's border ( $r = R$ ), it behaves as

$$a(r) \approx a_R + \mathcal{A}_R \rho^4 - \frac{2\mathcal{A}_R}{R} \rho^5, \quad r_0 < R, \quad (65)$$

for the internal impurity, and in the presence of the extended one reads

$$a(r) \approx a_R - \frac{g^2 R \Delta(R)}{N} \rho + \frac{g^2 [r_0^2 - (2d+1)R^2] \Delta(R)}{2N (r_0^2 - R^2)} \rho^2, \quad r_0 > R, \quad (66)$$

where  $\Delta(R)$  is given in (63) and the constant  $\mathcal{A}_R$  has been defined as

$$\mathcal{A}_R = \frac{3^3 R^4 g^2}{2^{14} \lambda^6 N^4 (1 + a_R)^3}. \quad (67)$$

Around the origin, the gauge field profiles behave according to Eq. (64), where we observe that the impurity parameter  $c$  affects the way the gauge field nears the origin, whereas the behavior close to the vacuum value  $a_R$  is given, respectively, by Eqs. (65) and (66) for the internal and extended impurities. We note that the internal impurity relatively does not alter the behavior of

the gauge profile around the vacuum. In contrast, the extended impurity modifies such behavior at first order in  $\rho$ . Aside from this, the new effects caused by the impurity are more accurately described by corresponding numerical solutions, as depicted in Fig. 4.

In particular, the left panel in Fig. 4 shows the gauge field profile in the presence of the internal impurity ( $r_0 < R$ ). We observe that for a  $c > 0$  and sufficiently large (here  $c > 1$ ), the profile  $a(r)$  is a monotonic increasing function from 0 up to a global maximum  $a_{\max} = a(r = r^*)$ , where  $0 < r^* < r_0$ , and then becomes a decreasing function with smooth approach to its vacuum value  $a_R$ , obeying (65). The black line represents  $c = 0$ , the compacton gauge field profile without a magnetic impurity. For  $c < 0$ , the admissible values lie in the interval  $c_{\min} < c < 0$ , where the gauge profiles monotonically decrease until they attain their vacuum values. In addition, we note compacton's radius decreases as  $c$  decreases towards the value  $c_{\min}$ , with  $a_R \rightarrow -1$  when  $c \rightarrow c_{\min}$ . Already in the right panel of Fig. 4, we have depicted the compact gauge profiles in the presence of an extended impurity ( $r_0 > R$ ). For  $c > 0$ , the allowed values lie in the interval  $0 < c < c_{\max}$  and thus, unlike the internal impurity, here the gauge profiles exhibit a global minimum when  $c \rightarrow c_{\max}$ . Again, the value  $c = 0$  (black line) provides the compact gauge profile without impurities. Lastly, for  $c < 0$ , the profile monotonically decreases towards its vacuum value obeying (66), with  $a_R \rightarrow -1$  when  $c$  assumes sufficiently large negative values. It is noteworthy that the existence of a maximum (internal impurity case) or a minimum (extended impurity case) on the gauge field  $a(r)$  profiles leads to the local flipping of the magnetic field, a fascinating feature we will discuss later.



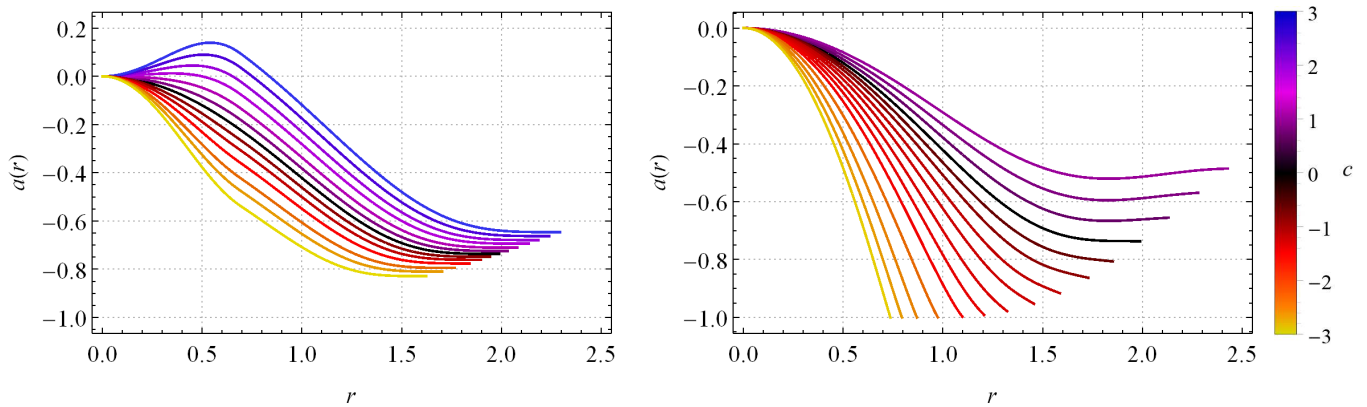


FIG. 4. Gauge field profiles  $a(r)$  obtained for the impurity function (56). Conventions as in Fig. 3.

#### 4. Magnetic field

For the total magnetic field  $B(r)$  we obtain the following expression around the origin,

$$B(r) \approx g^2(c-1) + g^2 \left( \frac{9}{2^5 \lambda^2 N} - \frac{cd}{r_0^2} \right) r^2 + \left[ \frac{g^2 cd(d-1)}{2r_0^4} - \frac{9g^4(c-1)}{2^7 N^2 \lambda^2} - \frac{3^3 g^2}{2^{10} N^2 \lambda^4} \right] r^4. \quad (68)$$

Besides, the behavior at the boundary  $r = R$  for the internal case reads as

$$B(r) \approx -\mathcal{B}_R \rho^3 + \frac{3\mathcal{B}_R}{2R} \rho^4, \quad r_0 < R, \quad (69)$$

which confirms the boundary conditions (18), with  $\mathcal{B}_R$  defined by

$$\mathcal{B}_R = \frac{3^3 g^2 R^3}{2^{12} \lambda^6 N^3 (1 + a_R)^3}. \quad (70)$$

Whereas, for the extended case, the behavior becomes

$$B(r) \approx g^2 \Delta(R) + \frac{2g^2 d R \Delta(R)}{r_0^2 - R^2} \rho - \frac{g^2 d [r_0^2 - (2d-1)R^2] \Delta(R)}{(r_0^2 - R^2)^2} \rho^2, \quad r_0 > R, \quad (71)$$

ensuring the boundary condition (31).

The behavior of the total magnetic field  $B(r)$  close to the frontiers is given by Eqs. (68), (69), and (71), being verified by the numerical solutions exhibited in Fig. 5. The left top panel shows the magnetic field profiles obtained in the presence of an internal impurity. Here, the numerical analysis shows a negative magnetic field for  $c_{\min} < c < 1$ , and according to (68), its amplitude at origin attains more negative values when  $c \rightarrow c_{\min}$ . Besides, within this interval, the first derivative of the

magnetic field changes its sign from positive to negative at the value

$$c \equiv \bar{c}_B = \frac{9r_0^2}{2^5 d \lambda^2 N}, \quad (72)$$

being here  $\bar{c}_B \simeq 0.106$ . It happens in the radial interval  $0 < r < r_0$ . On the other hand, for  $c > 1$ , the magnetic field at the origin is positive and remains so along a radial region  $0 \leq r < r_p$  (with  $r_p < r_0$ ) inside the impurity, besides for  $r_p < r < R$  the magnetic field is negative. In addition, the first derivative of the magnetic field is always positive for  $0 < r < r_0$  and negative for  $r > r_0$ . Therefore, the change of the magnetic field sign in the region  $0 \leq r < r_p$  implies a local magnetic flux flipping produced by the presence of the impurity. This phenomenon does not occur with the magnetic field of the BPS skyrmions engendered in the absence of the magnetic impurity. Note that this peculiar feature is a consequence of the behavior of the gauge field's  $a(r)$  discussed previously, where emerges a global maximum for  $c > 1$  values. Furthermore, one observes a behavior common to the profiles, which we can describe in the following way: they start from the origin, then quickly approach the impurity's radius  $r_0$  and so proceed monotonously to the vacuum value at the compacton border, in agreement with (69) and therefore satisfying (18).

In the right top panel of Fig. 5 are depicted the total magnetic field's profiles engendered in the presence of an extended impurity, whose radius here is fixed to be  $r_0 = 2.5$ . Thus, we have a magnetic field whose value at the origin is always negative due to the restriction  $c < c_{\max} \simeq 0.316 < 1$ , in agreement with (68), that is corroborated by calculating the value (72) that results in  $\bar{c}_B \simeq 1.352$ , a value outside the range of allowed values of  $c$ . Besides, the amplitude at the origin grows negatively for more negative values of  $c$ , whereas the compacton radius diminishes continuously. Further, as previously mentioned by discussing gauge field's profiles  $a(r)$ , we have the emergence of the global minimum when  $c \rightarrow c_{\max}$  engendering also a flipping of the magnetic field's sign (see the depiction inside in the right top panel of Fig.

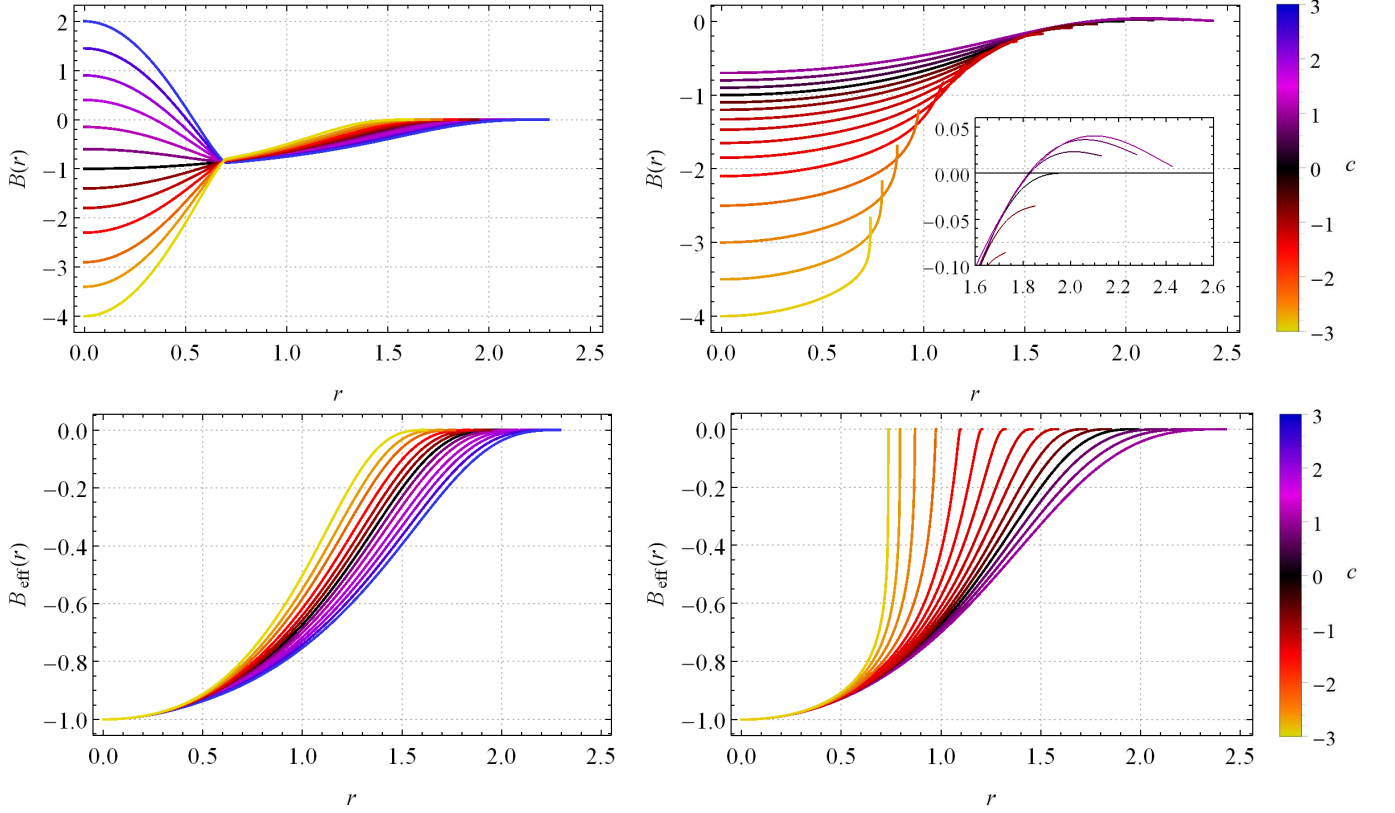


FIG. 5. The total magnetic field  $B(r)$  (top panels) and the corresponding effective magnetic field  $B_{\text{eff}}(r)$  (bottom panels), both obtained for the impurity function (56) by considering a fixed  $d = 1.3$  and different values of the parameter  $c$ . One has assumed  $r_0 = 0.7$  (left panels) for describe the internal impurity ( $r_0 < R$ ) and  $r_0 = 2.5$  (right panels) for represent the extended impurity ( $r_0 > R$ ). We also have fixed the values  $N = 1$ ,  $\lambda = 1$ , and  $g = 1$ .

5). Note that the profiles obey the behavior given in (71), which guarantees the boundary condition established by Eq. (31).

On the other hand, the effective magnetic field  $B_{\text{eff}}(r)$  defined in Eq. (32) at the origin behaves as

$$B_{\text{eff}}(r) \approx -g^2 + \frac{9g^2}{25\lambda^2 N} r^2 - \frac{9g^2}{27N^2\lambda^2} \left[ g^2(c-1) + \frac{3}{8\lambda^2} \right] r^4. \quad (73)$$

In contrast, at the border  $r = R$ , for the internal case, the effective magnetic field reads

$$B_{\text{eff}}(r) \approx -\mathcal{B}_R \rho^3 + \frac{3\mathcal{B}_R}{2R} \rho^4, \quad r_0 < R, \quad (74)$$

which has the same behavior as the total magnetic field happening because the own definition of the internal impurity introduced in Eq. (14). While, for the extended impurity, it approaches its vacuum value as

$$B_{\text{eff}}(r) \approx -\mathcal{B}_R \rho^3 + \frac{3\mathcal{B}_R}{2R} \left[ 1 - \frac{R^2 g^2 \Delta(R)}{N(1+a_R)} \right] \rho^4, \quad r_0 > R, \quad (75)$$

where  $\mathcal{B}_R$  is given in Eq. (70). Here, we observe the contribution from the impurity appearing at higher orders, albeit in the internal case, it does not affect at least the same order.

The effective magnetic field's profiles are shown in the bottom panels in Fig. 5. The profiles are well-behaved around the origin for both impurity types, in agreement with (73). In general, the profile format follows a similar behavior to the one emerging in the absence of impurity. Nevertheless, the impurity affects the size of the compactons, i.e., their radii, as shown by the bottom panels in Fig. 5. Specifically, the radius of the compactor decreases as  $c$  grows negatively in the presence of both the internal and extended impurity, such as previously observed through Fig. 1. The diminishing of the compacton's radius can be related to the reduction in the area occupied by the magnetic field, thus impacting the total magnetic flux carried by the defect.

### 5. BPS energy density

The corresponding BPS energy density (47), for the superpotential (54) and impurity function (56), behaves

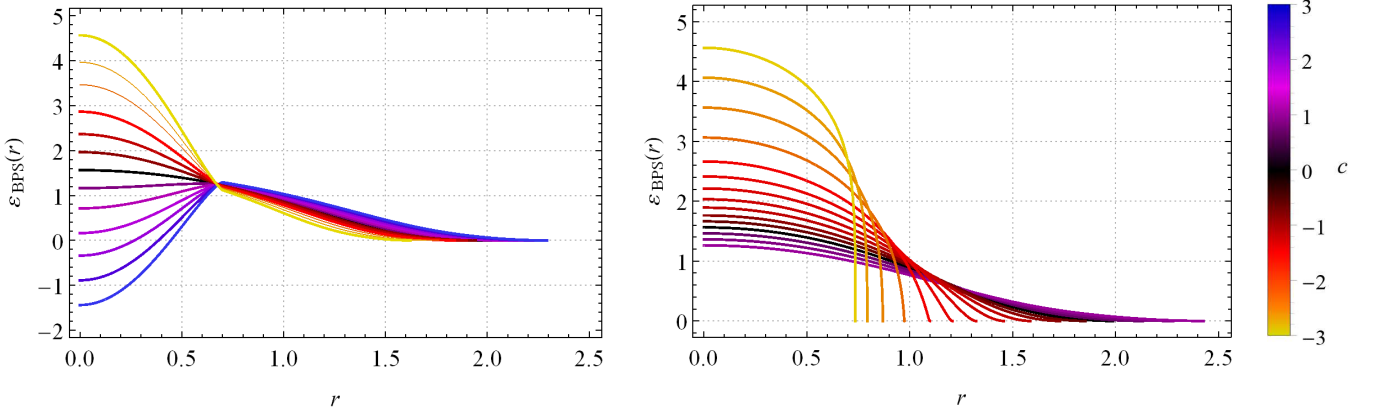


FIG. 6. The profiles of the BPS energy density  $\varepsilon_{\text{BPS}}(r)$  obtained for the impurity function (56). Conventions as in Fig. 3.

near the origin as

$$\varepsilon_{\text{BPS}} \approx \frac{9}{2^4 \lambda^2} - g^2(c-1) - \left[ \frac{3^3}{2^8 N \lambda^4} - \frac{9g^2(c-2)}{2^5 N \lambda^2} - \frac{cdg^2}{r_0^2} \right] r^2. \quad (76)$$

Moreover, at the compacton's border, for the internal case reads as

$$\varepsilon_{\text{BPS}} \approx \mathcal{E}_R \rho^2 - \frac{\mathcal{E}_R}{R} \rho^3, \quad r_0 < R, \quad (77)$$

whereas for the extended impurity behaves as

$$\varepsilon_{\text{BPS}} \approx \mathcal{E}_R \rho^2 - \frac{\mathcal{E}_R}{R} \left[ 1 - \frac{2R^2 g^2 \Delta(R)}{3N(1+a_R)} \right] \rho^3, \quad r_0 > R, \quad (78)$$

where we have defined  $\mathcal{E}_R$  by

$$\mathcal{E}_R = \frac{3^4 R^2}{2^{12} \lambda^6 N^2 (1+a_R)^2}. \quad (79)$$

Such as, in the case of the magnetic field profiles, the impurity's parameters only emerge at high orders in  $\rho = R - r \rightarrow 0^+$ .

Figure 6 depicts the numerical profiles of the BPS energy density (47), so the left panel shows the ones obtained in the presence of an internal impurity, and the right panel depicts the profiles emerging when an extended impurity is present. One can better understand the profiles' format by looking at the behavior given in Eq. (76) and by its first derivative. Firstly, we see that the amplitude at the origin becomes null when  $c$  attains the value

$$c \equiv \bar{c}_\varepsilon = 1 + \frac{9}{2^4 \lambda^2 g^2}, \quad (80)$$

independent of the impurity's parameters  $d$  and  $r_0$ . Besides, the first derivative of (76) at the origin changes its

sign, i.e., the second derivative becomes null em  $r = 0$  when  $c$  assumes the value

$$\bar{c}_\varepsilon = \frac{9(2^4 g^2 \lambda^2 + 3)r_0^2}{8\lambda^2 g^2 (2^5 N d \lambda^2 + 9r_0^2)}, \quad (81)$$

which now depends on the impurity's parameters  $d$  and  $r_0$ . This way, for the parameter values chosen to perform the numerical analysis, the value (80) is  $\bar{c}_\varepsilon \simeq 1.563$  that belongs to the range  $c > c_{\text{min}} \simeq -7.631$  of the values allowed for the case of the internal impurity ( $r_0 = 0.7$ ). It explains the change in sign of the amplitude of the BPS energy density at the origin when  $c$  grows (see the left panel in Fig. 6). On the other hand, in the presence of the extended impurity ( $r_0 = 2.5$ ), the value  $\bar{c}_\varepsilon \simeq 1.563$  is outside the interval  $c < c_{\text{max}} \simeq 0.316$  of the permitted values, therefore, in this case, the amplitude at the origin never be null, such as shown by the right panel of the Fig. 6. Likewise, in the case of the internal impurity ( $r_0 = 0.7$ ), the concavity, or the convexity of the profiles of the BPS energy density, in the interval  $0 \leq r < r_0$ , is explained by the value (81), which here is  $\bar{c}_\varepsilon \simeq 0.228 > c_{\text{min}} \simeq -7.631$ , subsequently for  $c_{\text{min}} < c < 0.228$  the profiles are concave and for  $c > 0.228$  they are convex. In contrast, in the presence of the extended impurity ( $r_0 = 2.5$ ) the value (81) becomes  $\bar{c}_\varepsilon \simeq 1.365$  resulting be greater than the maximum allowed value  $c_{\text{max}} \simeq 0.316$ , consequently, the profiles are concave for all permitted values  $c < c_{\text{max}}$ , such as observed in the right panel of Fig. 6.

## 6. Magnetic flux

The total magnetic flux  $\Phi_B$ , given in (49), is proportional to  $a_R$  defined in Eq. (50), which becomes

$$a_R = -1 + \exp\left(-\frac{4}{3}g^2\lambda^2 - g^2 I_\Delta\right), \quad (82)$$

and by regarding the superpotential (54), we have calculated (51) to obtain  $I_W = 4/3$ . From (52), the quantity

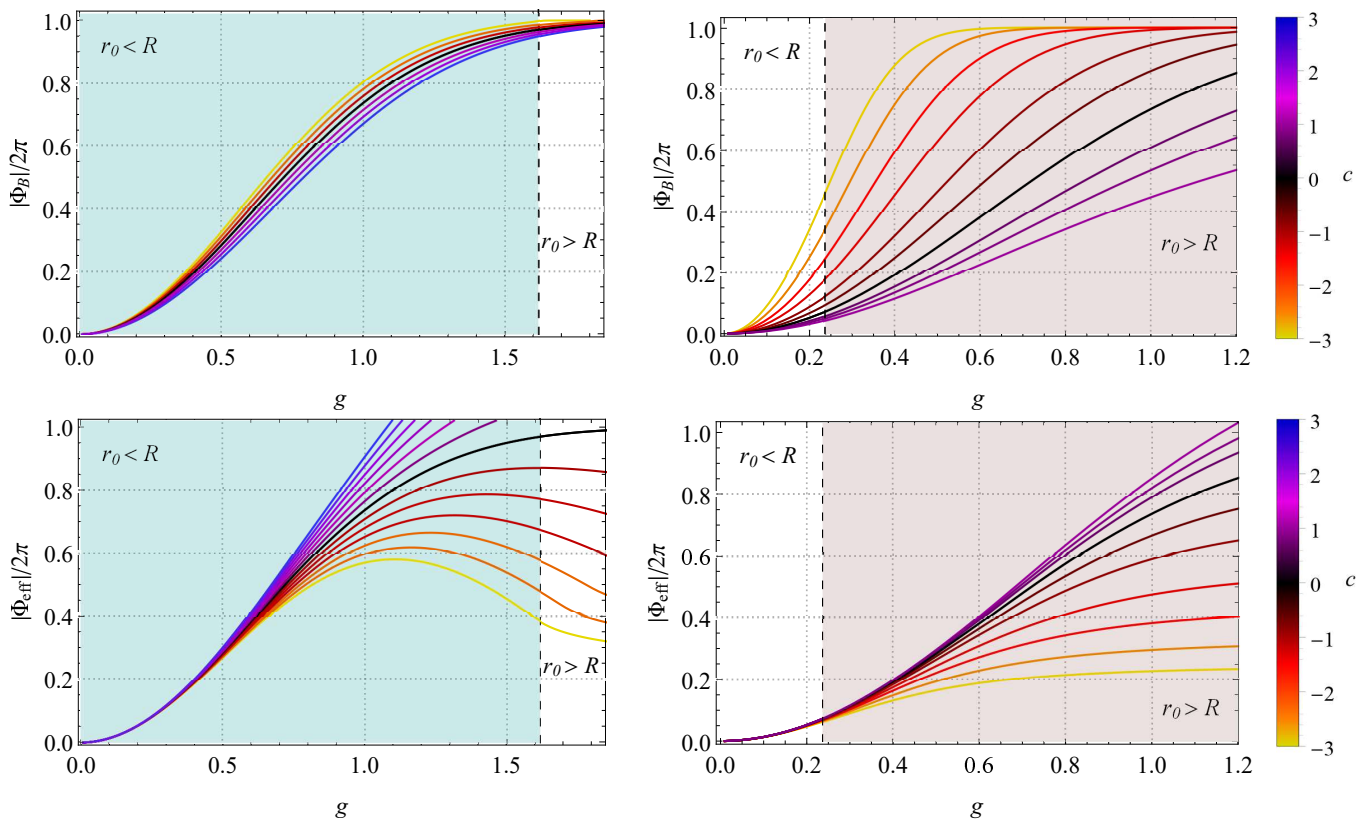


FIG. 7. The total flux magnetic  $\Phi_B$  (top panels) and the corresponding effective magnetic flux  $\Phi_{\text{eff}}$  (bottom panels) are both displayed as functions of the electromagnetic coupling  $g$  for the impurity function (56) when one fixes  $d = 1.3$  and runs the  $c$  values. Besides, the internal impurity possesses a radius  $r_0 = 0.6$  (left panels), and the extended has a radius  $r_0 = 3.5$  (right panels). We also have fixed the values  $N = 1$  and  $\lambda = 1$ .

$I_\Delta$  given by

$$I_\Delta = c \frac{8\lambda^2}{3} \int_0^R \left(1 - \frac{r^2}{r_0^2}\right)^d \frac{\theta(r_0 - r)}{\sqrt{h}} \frac{dh}{dr} dr, \quad (83)$$

will be calculated numerically to perform the magnetic flux analysis.

For our purpose, in the top panels of Fig. 7, we have depicted the absolute value of the total magnetic flux  $\Phi_B$  given by (49) as a function of  $g$  for different  $c$  values. With a loss of generality, we present the total flux in the presence of both the internal impurity (here with radius  $r_0 = 0.6$ , on the left panel) and the extended one (here with radius  $r_0 = 3.5$ , on the right panel). We observe that for sufficiently large  $g$ , and  $c \rightarrow \bar{c}_{\min} = -3.0$  in the internal case or for  $c < \bar{c}_{\max} = 0.3$  and growing negatively when the case of the extended impurity, the quantity  $a_R \rightarrow -1$  then  $\Phi_B \rightarrow -2\pi$ , which becomes quantized in units of  $2\pi$ . Additionally, we have highlighted in the figure the interval  $0 < g < g_{\max} \simeq 1.619$  that for the internal impurity defines the allowed values engendering compact Skyrmions possessing a radius  $R$  satisfying the condition  $R > r_0$  that ensuring that the boundary conditions established in Eqs. (16), (17), and (18) be satisfied. Similarly, in the presence of an extended impurity, we identified the range  $g > g_{\min} \simeq 0.238$  that

TABLE I. Values for the electromagnetic coupling constant in the presence of the magnetic impurity.

Internal impurity <sup>a</sup>		Extended impurity <sup>b</sup>	
$r_0$	$g_{\max}$	$r_0$	$g_{\min}$
1.0	1.005	3.5	0.238
0.7	1.403	3.0	0.635
0.6	1.619	2.5	0.989
0.4	2.370	2.0	1.282
0.3	3.133	1.5	1.545

We have fixed <sup>a</sup> $\bar{c}_{\min} = -3.0$  for internal impurity and <sup>b</sup> $\bar{c}_{\max} = 0.3$  for extended impurity, by setting  $N = 1$ ,  $\lambda = 1$ , and  $d = 1.3$ .

represents the permitted  $g$  values generating compactons whose radii fulfilling the condition  $R < r_0$  so guaranteeing the boundary conditions (16), (30), and (31) be satisfied too. Moreover, we have also depicted the effective magnetic flux (36) for both impurity scenarios in the bottom panels of Fig. 7.

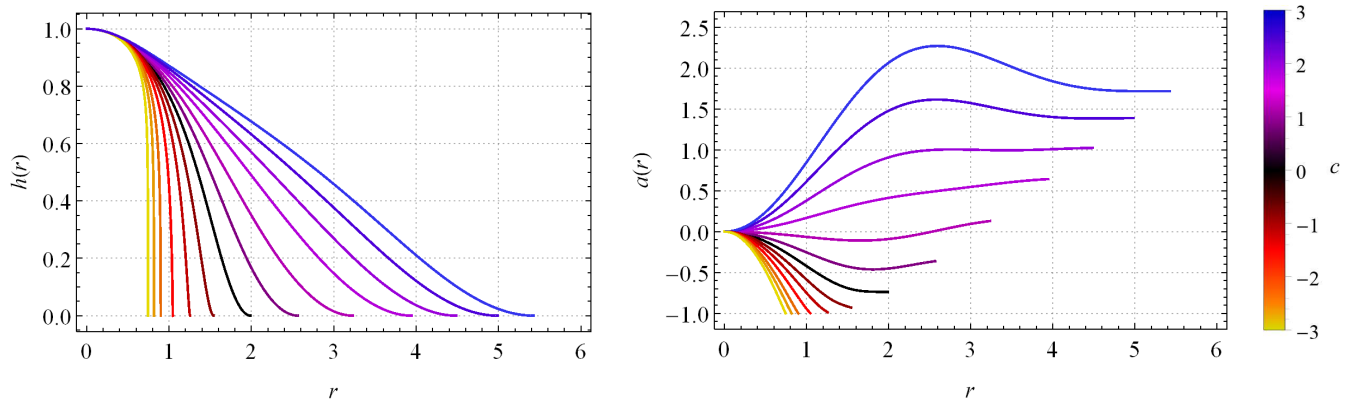


FIG. 8. The Skyrmon profiles  $h(r)$  (left panel) and the gauge field profiles  $a(r)$  (right panel), both obtained for the impurity function (84) when one sets  $\sigma = 1.3$  and runs the values of the parameter  $c$ . We also have fixed the values  $N = 1$ ,  $\lambda = 1$ , and  $g = 1$ .

### 7. Effects of the magnetic impurity on the electromagnetic coupling constant

In the gauged BPS baby Skyrme model [33], the electromagnetic coupling constant  $g$  controls the compacton's size. A similar situation happens in our model, where we perceive that besides the coupling constant  $g$  to control the compacton's size, the impurity parameters also do it. Thus, one perceives a relationship between the coupling constant  $g$  allowed values and the impurity parameters, according to the constraints rising due to the boundary conditions established for both the internal and extended impurity case.

We provide the table I to understand such a relationship better. We observe that the electromagnetic coupling constant has restricted values depending on whether the impurity is internal or extended, which is entirely characterized by the impurity radius  $r_0$ . In this sense, by convenience, we have fixed the value  $\bar{c}_{\min}$  such that for the internal impurity, the values  $c > \bar{c}_{\min}$  are permitted. On the other hand, in the case of the extended impurity, we have fixed  $\bar{c}_{\max}$  such that the values  $c < \bar{c}_{\max}$  are the ones allowed. This way, for the numerical analysis, we also set  $N = 1$ ,  $\lambda = 1$ , and  $d = 1.3$ . Consequently, we observe that once the radius  $r_0$  of the internal impurity is choice, there exists a maximum value  $g_{\max}$  of the electromagnetic coupling constant such that for  $g < g_{\max}$ , the condition  $r_0 < R$  remains valid and the compacton achieve the boundary conditions established in Eqs. (16), (17), and (18). Similarly, when we consider an extended impurity with a selected radius  $r_0$ , the electromagnetic coupling constant attains a minimum value  $g_{\min}$  such that for  $g > g_{\min}$  the condition  $r_0 > R$  is achieved. So, the compacton enforces the boundary conditions established in Eqs. (16), (30), and (31). As an example, it is interesting to analyze total magnetic flux  $\Phi_B$  (see Fig. 7) and see how the impurity parameters restrain the  $g$  allowed values. For our purpose, we have adopted an internal impurity (left panel) with radius  $r_0 = 0.6$ ,

which fixes for  $g$  the maximum value  $g_{\max} \simeq 1.619$  (see table I), represented by region  $r_0 < R$ . Regarding the extended case (right panel), we have chosen  $r_0 = 3.5$ , achieving for  $g$  the minimum value  $g_{\min} \simeq 0.238$  (see table I) represented by region  $r_0 > R$ .

### B. Gaussian impurity

We now continue our analysis by choosing a Gaussian impurity defined as

$$\Delta(r) = c \exp\left(-\frac{r^2}{2\sigma^2}\right), \quad (84)$$

where  $c \in \mathbb{R}$  and  $\sigma > 0$  are constants that control the amplitude and the effective width, respectively. The impurity (84) will be analyzed via our approach described in Sec. III B. Concerning the study of topological defects in the presence of magnetic impurities, the Gaussian function has already been previously used, for example, in Refs. [58, 66].

The profiles  $h(r)$  of the Skyrme field are shown in the left panel of Fig. 8. They also behaves around the origin according Eq. (59) whereas near the compacton's boundary, i.e., when  $\rho = R - r \rightarrow 0^+$ , the profiles comport as the given by Eq. (61), where  $\Delta(R)$  now reads as

$$\Delta(R) = c \exp\left(-\frac{R^2}{2\sigma^2}\right) = \lim_{r \rightarrow R} \Delta(r). \quad (85)$$

The numerical analysis shows that for  $c \geq 0$ , the profiles attain the vacuum value in a smoothing way such that the compacton's radius is longer than the one without impurity. Conversely, for  $c < 0$ , they achieve the vacuum value quickly, and simultaneously, the compacton's radius will be shorter than the one without impurity.

Similarly, the right panel of Fig. 8 depicts the gauge field profiles  $a(r)$ . The behavior near the origin reads as

$$a(r) \approx \frac{g^2(c-1)}{2N}r^2 + \frac{g^2}{4N} \left( \frac{9}{2^5 \lambda^2 N} - \frac{c}{2\sigma^2} \right) r^4, \quad (86)$$

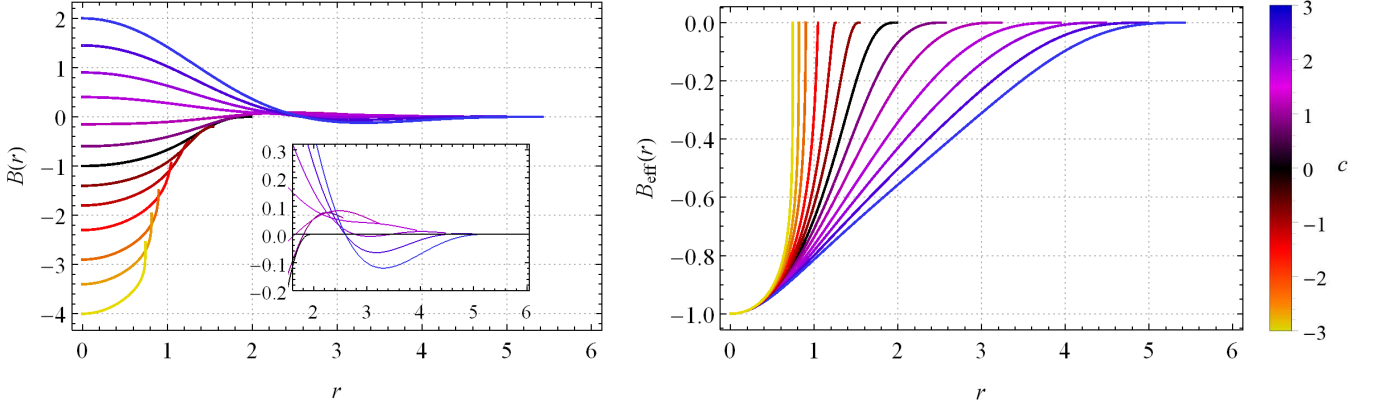


FIG. 9. The total magnetic field  $B(r)$  (left panel) and the corresponding effective magnetic field  $B_{\text{eff}}(r)$  (right panel), both obtained for the impurity function (84). Conventions as in Fig. 8.

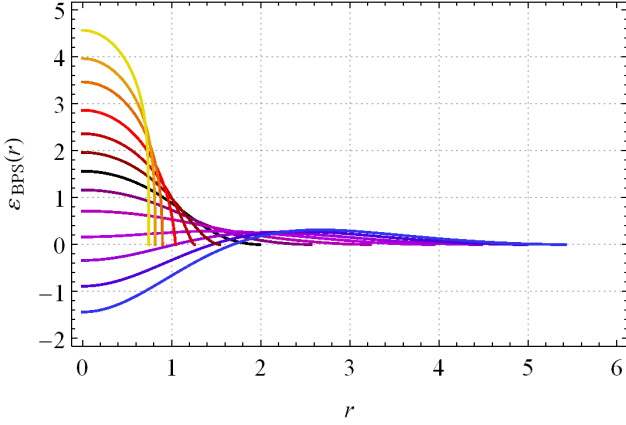


FIG. 10. The profiles of the BPS energy density  $\varepsilon_{\text{BPS}}(r)$  obtained for the impurity function (84). Conventions as in Fig. 8.

which clarifies why the profiles exhibit a convex format for  $c > 1$  and a concave shape for  $c < 1$ . In addition, the profile behavior near the compacton's border becomes

$$a(r) \approx a_R - \frac{g^2 R \Delta(R)}{N} \rho - \frac{g^2 (R^2 - \sigma^2) \Delta(R)}{2N\sigma^2} \rho^2. \quad (87)$$

The numerical solutions also show that the impurity noticeably affects the  $a(r)$  profiles by promoting the emergence of a global maximum for  $c > 0$  and a global minimum for  $c < 0$ .

Figure 9 presents the magnetic field profiles (left panel). We observe that the amplitude at  $r = 0$  has negative values for  $c < 1$  and turns positive when  $c > 1$ , as can be verified by the behavior around the origin shown to follow

$$B(r) \approx g^2(c-1) + g^2 \left( \frac{9}{32\lambda^2 N} - \frac{c}{2\sigma^2} \right) r^2 + \left[ \frac{g^2 c}{8\sigma^4} - \frac{9g^4(c-1)}{2^7 N^2 \lambda^2} - \frac{3^3 g^2}{2^{10} N^2 \lambda^4} \right] r^4. \quad (88)$$

It also allows us to explain that for the  $c < 9\sigma^2/(16N\lambda^2)$  (here  $\sim 0.951$ ), the magnetic field around the origin acquires a convex format, whereas for  $c > 9\sigma^2/(16N\lambda^2)$  it presents a concave layout. Besides, for  $c < 1$ , the magnetic field profiles present a format like the ones engendered by the extended impurity studied in section IV A 4 (see the top right panel of Fig. 5), with the tails also exhibit the flipping of the magnetic field before achieving the vacuum value. Already, for  $c > 1$ , the profiles possess a layout like the ones observed in the presence of an internal impurity described in the section IV A 4 (see the top left panel of Fig. 5), with the tails now show the inverting the magnetic field before reaching the vacuum value. The flipping of the magnetic field tail is observed through the profile behavior when  $r \rightarrow R$ , reading as

$$B(r) \approx g^2 \Delta(R) + \frac{g^2 R \Delta(R)}{\sigma^2} \rho + \frac{g^2 (R^2 - \sigma^2) \Delta(R)}{2\sigma^4} \rho^2, \quad (89)$$

[with  $\Delta(R)$  defined in Eq. (85)] which also confirms the boundary condition (31).

The right panel of Fig. 9 shows the effective magnetic field. The profiles behave at  $r = 0$  as given by Eq. (73), which, as expected, tells us the magnetic field amplitude at the origin is constant and will always have a convex format all around the neighborhood. It happens because the impurity does not significantly affect the profiles around the origin, i.e., they behave similarly to that obtained without impurity. The principal effect coming from the impurity is changes in the length of the compacton's radius, indeed, it becomes minor whenever  $c$  acquires more negative values and turns bigger for increasing positive values of  $c$ . Moreover, the tail behaves like the one obtained in the impurity's absence, being described by Eq. (75); this way, it suggests that the tail of the effective magnetic field does not flip.

Figure 10 displays the profiles of the BPS energy den-

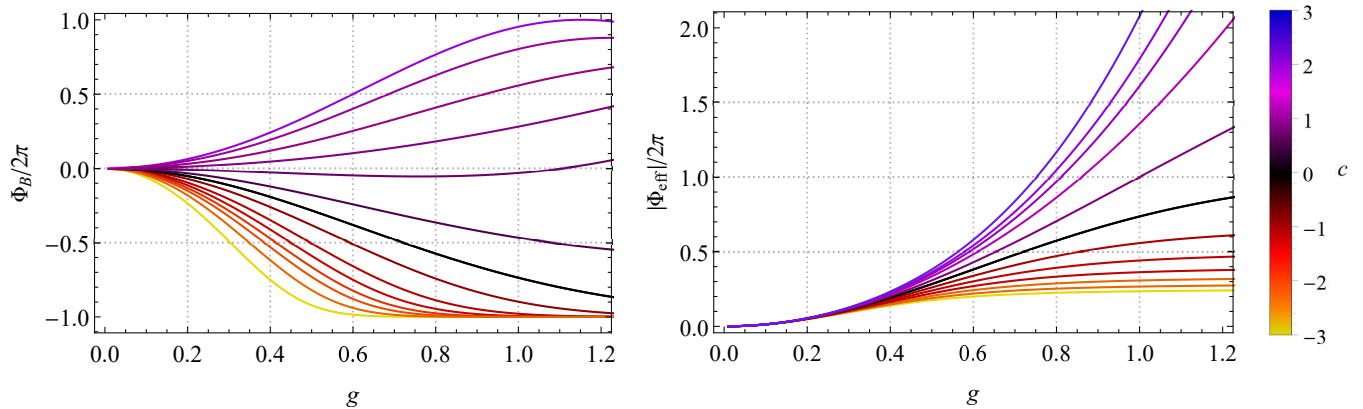


FIG. 11. The total flux magnetic  $\Phi_B$  (left panel) and the corresponding effective magnetic flux  $\Phi_{\text{eff}}$  (right panel) are both represented as functions of the electromagnetic coupling  $g$  for the impurity function (84) when one set  $\sigma = 1.3$  and runs the  $c$  values. We also have fixed the values  $N = 1$  and  $\lambda = 1$ .

sity whose respective behaviors at  $r = 0$  read as

$$\varepsilon_{\text{BPS}} \approx \frac{9}{2^4 \lambda^2} - g^2(c-1) - \left[ \frac{27}{2^8 N \lambda^4} - \frac{9g^2(c-2)}{2^5 N \lambda^2} - \frac{cg^2}{2\sigma^2} \right] r^2. \quad (90)$$

It illuminates why the BPS energy density's amplitude at  $r = 0$  changes its signal when  $c \neq \bar{c}_\varepsilon$  (here  $\bar{c}_\varepsilon \simeq 1.563$ ) in according to Eq. (80). Similarly, the second derivative is null when  $c$  assumes the value

$$c_G = \frac{9(2^4 g^2 \lambda^2 + 3)\sigma^2}{2^3 g^2 \lambda^2 (9\sigma^2 + 2^4 N \lambda^2)}. \quad (91)$$

This way, around the origin's neighborhood, the profile possesses a convex format for  $c > c_G$  (here  $c_G \sim 1.157$ ) and gains a concave layout for  $c < c_G$ . Furthermore, for  $\rho = R - r \rightarrow 0^+$ , the BPS energy density obeys the same expression in Eq. (78). So despite, near to the origin, it has a negative value for  $c > \bar{c}_\varepsilon$ , the profiles suffer an inversion such that the tails always approach the vacuum values maintaining a positive signal.

Finally, we have presented in Fig. 11 the profiles of the total (left panel) and practical (right panel) magnetic flux, respectively, for fixed  $\sigma$ , as functions of the electromagnetic coupling  $g$  and the  $c$  parameter. The total magnetic flux  $\Phi_B$  is negative for positive small values of  $c$ ; in contrast, for sufficiently large positive  $c$ , it becomes positive such that for increasing values of  $c$  and  $g$ , the gauge vacuum value,  $a_R \rightarrow 1$  then  $\Phi_B \rightarrow 2\pi$ . On the other hand, for  $c < 0$ , the magnetic flux is always negative, and for sufficiently large negative  $c$  values and large enough  $g$ ,  $a_R \rightarrow -1$  thus  $\Phi_B \rightarrow -2\pi$ . Such a situation contrasts totally with the case of the finite-sized impurity (56) [see the top panels in Fig. 7] where the vacuum value  $a_R$  always goes to  $-1$  such that  $\Phi_B \rightarrow -2\pi$ . On the other hand, the effective magnetic flux  $\Phi_{\text{eff}}$  comports very similar to the one described by the previous scenario defined by the impurity (56) [see the bottom panels in Fig. 7].

## V. REMARKS AND CONCLUSIONS

We have investigated the emergence of BPS compactons in the gauged restricted baby Skyrme model interacting with a magnetic impurity. For such a purpose, we have focused on constructing the BPS structure, which allows us to achieve the BPS equations whose solutions saturate the Bogomol'nyi bound and set the self-dual potential. While implementing the BPS formalism, one has perceived that the construction depends on the relative size between the compacton and the impurity. To perform such an analysis, we consider two scenarios: the first considers the impurity wholly inside the compacton, and the second regards the compacton entirely within the impurity. Despite both situations, the Bogomol'nyi bound, self-dual equations, and inclusive potential remain the same in both scenarios. For an impurity that satisfies the constraints given in Eq. (14) or Eq. (29), the requirement of the compacton possessing finite total energy leads to imposing that the energy density being null at the compacton border. This condition changes the boundary conditions satisfied by the magnetic field and the potential, such as verified when comparing Eqs. (18) and (31).

To deepen the study, we have selected two types of magnetic impurities. The first has a finite size (step-type function), and the second extends along the radial axis (Gaussian function). The analysis of the step-type impurity (Sec. IV A) reveals that the amplitude  $c$  has a lower limit for the internal case and an upper limit for the extended case. Furthermore, the gauge field profile leaves its monotonic behavior, which now can present a maximum (in the internal case) and a minimum (in the extended case), implying a magnetic field flipping (top panels in Fig. 5), a significant feature indicating the magnetic flux local inversion phenomenon. In addition, a detailed analysis of the magnetic flux dependence on the electromagnetic coupling constant has shown that  $g$  has restricted values depending on whether the impurity is

internal or extended (see Fig. 7 and table I). In contrast to the first scenario, the Gaussian impurity (Sec. IV B) belonging to the extended case does not present a limitation for the values of the amplitude  $c$  nor the values of the electromagnetic coupling constant. On the other hand, some features become common here; for example, the compacton's radius changes its size with the impurity amplitude, playing a similar role as the electromagnetic coupling constant. Besides, the total magnetic flux remains nonquantized, as in the case without impurity. Still, adjusting the parameters to attain a magnetic flux quantized in units of  $2\pi$  becomes possible. These findings are of utmost importance, as they provide crucial insights into the behavior of the BPS compact Skyrmons in the presence of a finite- or infinite-sized impurity.

Finally, it is worthwhile to point out that our formalism, applied here to investigate compact Skyrmons, is also valuable for studying non-compact solutions with tails decaying with Gaussian or power law.

We currently investigate BPS structures' existence in generalized or effective versions of the gauged restricted baby Skyrme model. The exploring includes nonstandard kinetic terms for both the gauge and Skyrme fields. Fur-

thermore, by including the Chern-Simons term, we are conducting studies to examine the electric and magnetic properties of the gauged baby Skyrme model in the presence of impurities. We will report the results concerning these studies in future contributions.

## ACKNOWLEDGMENTS

This study was financed in part by the Coordenação de Aperfeiçoamento de Pessoal de Nível Superior - Brasil (CAPES) - Finance Code 001. We thank also the Conselho Nacional de Desenvolvimento Científico e Tecnológico (CNPq), and the Fundação de Amparo à Pesquisa e ao Desenvolvimento Científico e Tecnológico do Maranhão (FAPEMA) (Brazilian Government agencies). In particular, N. H. G. G. thanks the full support from CAPES; R. C. acknowledges the support from the grants CNPq/312155/2023-9, FAPEMA/UNIVERSAL-00812/19, and FAPEMA/APP-12299/22; A. C. S. thank the grants CAPES/88882.315461/2019-01 and CNPq/150402/2023-6.

- 
- [1] T. H. R. Skyrme, Proc. R. Soc. London **260**, 127 (1961); Nucl. Phys. **31**, 556 (1962).
- [2] I. Zahed and G. E. Brown, Phys. Rept. **142**, 1 (1986).
- [3] G. S. Adkins, C. R. Nappi, and E. Witten, Nucl. Phys. B **228**, 552 (1983).
- [4] G. S. Adkins and C. R. Nappi, Nucl. Phys. B **233**, 109 (1984).
- [5] O. V. Manko, N. S. Manton, and S. W. Wood, Phys. Rev. C **76**, 055203 (2007).
- [6] R. A. Battye, N. S. Manton, P. M. Sutcliffe, and S. W. Wood, Phys. Rev. C **80**, 034323 (2009).
- [7] P. H. C. Lau and N. S. Manton, Phys. Rev. Lett. **113**, 232503 (2014).
- [8] C. J. Halcrow, Nucl. Phys. B **904**, 106 (2016).
- [9] C. J. Halcrow, C. King, and N. S. Manton, Phys. Rev. C **95**, 031303 (2017).
- [10] Y.-L. Ma, M. Harada, H. K. Lee, Y. Oh, B.-Y. Park, and M. Rho, Phys. Rev. D **88**, 014016 (2013); Phys. Rev. D **88**, 079904(E) (2013).
- [11] M. Harada, H. K. Lee, Y.-L. Ma and M. Rho, Phys. Rev. D **91**, 096011 (2015).
- [12] Y.-L. Ma and M. Rho, Sci. China Phys. Mech. Astron. **60**, 032001 (2017).
- [13] J. W. Holt, M. Rho and W. Weise, Phys. Rept. **621**, 2 (2016).
- [14] C. Adam, C. Naya, J. Sanchez-Guillen, R. Vazquez, and A. Wereszczynski, Phys. Lett. B **742**, 136 (2015); Phys. Rev. C **92**, 025802 (2015).
- [15] S. Nelmes and B. M. A. G. Piette, Phys. Rev. D **84**, 085017 (2011); Phys. Rev. D **85**, 123004 (2012).
- [16] C. Naya and P. Sutcliffe, Phys. Rev. Lett. **121**, 232002 (2018).
- [17] E. Bogomol'nyi, Sov. J. Nucl. Phys. **24**, 449 (1976).
- [18] M. Prasad and C. Sommerfield, Phys. Rev. Lett. **35**, 760 (1975).
- [19] E. Bonenfant and L. Marleau, Phys. Rev. D **82**, 054023 (2010).
- [20] P. Sutcliffe, J. High Energ. Phys. **2010**, 19 (2010); **2011**, 45 (2011).
- [21] E. Bonenfant, L. Harbour, and L. Marleau, Phys. Rev. D **85**, 114045 (2012).
- [22] S. B. Gudnason, M. Barsanti, and S. Bolognesi, J. High Energy Phys. **2020**, 62 (2020); **2022**, 92 (2022).
- [23] S. B. Gudnason and C. Halcrow, Phys. Lett. B **850**, 138526 (2024).
- [24] B. M. A. G. Piette, B. J. Schroers, and W. J. Zakrzewski, Z. Phys. C **65**, 165 (1995); Nucl. Phys. B **439**, 205 (1995).
- [25] R. A. Leese, M. Peyrard, and W. J. Zakrzewski, Nonlinearity **3**, 773 (1990).
- [26] B. Piette and W. J. Zakrzewski, Chaos Solit. Fractals **5**, 2495 (1995).
- [27] A. Kudryavtsev, B. M. A. G. Piette and W. J. Zakrzewski, Eur. Phys. J. C **1**, 333 (1998).
- [28] T. Gisiger and M. B. Paranjape, Phys. Lett. B **384**, 207 (1996).
- [29] T. Gisiger and M. B. Paranjape, Phys. Rev. D **55**, 7731 (1997).
- [30] C. Adam, T. Romanczukiewicz, J. Sanchez-Guillen, and A. Wereszczynski, Phys. Rev. D **81**, 085007 (2010).
- [31] O. Alvarez, L. A. Ferreira, and J. Sanchez-Guillen, Nucl. Phys. B **529**, 689 (1998); Int. J. Mod. Phys. A **24**, 1825 (2009).
- [32] J. M. Speight, J. Phys. A **43**, 405201 (2010).
- [33] C. Adam, C. Naya, J. Sanchez-Guillen, and A. Wereszczynski Phys. Rev. D **86**, 045010 (2012).
- [34] C. Adam and A. Wereszczynski, Phys. Rev. D **95**, 116006 (2017).
- [35] R. Casana and A. C. Santos, Phys. Rev. D **101**, 065009 (2020).



- (2021).
- [36] J. Andrade, R. Casana, E. da Hora, and A. C. Santos, *Phys. Rev. D* **110**, 056005 (2024).
- [37] C. A. I. Florián, R. Casana, and A. C. Santos, *Ann. Phys.* **470**, 169820 (2024).
- [38] C. Adam, C. Naya, J. Sanchez-Guillen, and A. Wereszczynski, *J. High Energ. Phys.* **2013**, 12 (2013)
- [39] R. Casana, A. C. Santos, C. F. Farias and A. L. Mota, *Phys. Rev. D* **101**, 045022 (2019).
- [40] R. Casana, A. C. Santos, C. F. Farias and A. L. Mota, *Phys. Rev. D* **101**, 045018 (2020).
- [41] S. B. Gudnason, M. Nitta, and S. Sasaki. *J. High Energ. Phys.* **2016**, 74 (2016).
- [42] M. Nitta and S. Sasaki, *Phys. Rev. D* **91**, 125025 (2015).
- [43] C. Adam, J.M. Queiruga, J. Sanchez-Guillen, and A. Wereszczynski, *J. High Energ. Phys.* **2013**, 108 (2013).
- [44] J. M. Queiruga, *J. Phys. A* **52**, 055202 (2019).
- [45] C. Adam, T. Romanczukiewicz, M. Wachla, and A. Wereszczynski, *J. High Energ. Phys.* **2018**, 97 (2018).
- [46] M. Wachla, *Phys. Rev. D* **99**, 065006 (2019).
- [47] T. Shapoval, V. Metlushko, M. Wolf, B. Holzapfel, V. Neu, and L. Schultz, *Phys. Rev. B* **81**, 092505 (2010).
- [48] S. Tung, V. Schweikhard, and E. A. Cornell, *Phys. Rev. Lett.* **97**, 240402 (2006).
- [49] A. Griffin, G. W. Stagg, N. P. Proukakis, and C. F. Barengi, *J. Phys. B* **50**, 115003 (2017).
- [50] P.W. Anderson and N. Itoh, *Nature* **256**, 25 (1975).
- [51] G. Wlazlowski, K. Sekizawa, P. Magierski, A. Bulgac, and M. M. Forbes, *Phys. Rev. Lett.* **117**, 232701 (2016).
- [52] C. Adam and A. Wereszczynski, *Phys. Rev. D* **98**, 116001 (2018).
- [53] C. Adam, T. Romanczukiewicz, and A. Wereszczynski, *J. High Energy Phys.* **2019**, 131 (2019).
- [54] C. Adam, K. Oles, J. M. Queiruga, T. Romanczukiewicz, and A. Wereszczynski, *J. High Energ. Phys.* **2019**, 150 (2019).
- [55] C. Adam, J. M. Queiruga, and A. Wereszczynski, *J. High Energ. Phys.* **2019**, 164 (2019).
- [56] D. Tong and K. Wong, *J. High Energy Phys.* **2014**, 90 (2014).
- [57] X. Han and Y. Yang, *J. High Energy Phys.* **2016**, 46 (2016).
- [58] V. Almeida, R. Casana, E. da Hora, and S. Krusch, *Phys. Rev. D* **106**, 016010 (2022).
- [59] J. E. Ashcroft and S. Krusch, *Phys. Rev. D* **101**, 025004 (2020).
- [60] E. Witten and D. Olive, *Phys. Lett. B* **78**, 97 (1978).
- [61] Z. Hlousek and D. Spector, *Nucl. Phys. B* **370**, 143 (1992); *Nucl. Phys. B* **397**, 173 (1993).
- [62] C. Adam, J. M. Queiruga, J. Sanchez-Guillen and A. Wereszczynski, *J. High Energ. Phys.* **2013**, 108 (2013).
- [63] C. Adam, T. Romanczukiewicz, J. Sanchez-Guillen, and A. Wereszczynski, *J. High Energ. Phys.* **2014**, 95 (2014).
- [64] C. Adam, C. Naya, T. Romanczukiewicz, J. Sanchez-Guillen, and A. Wereszczynski, *J. High Energ. Phys.* **2015**, 155 (2015).
- [65] C. Adam, P. Klimas, J. Sánchez-Guillén, and A. Wereszczynski, *Phys. Rev. D* **80**, 105013 (2009)
- [66] J. Ashcroft and S. Krusch, *Phys. Rev. D* **101**, 025004 (2020).